Materials Views
www.MaterialsViews.com

ADVANCED FUNCTIONAL MATERIALS
www.afm-journal.de

Photovoltaic Effect at the Schottky Interface with Organic Single Crystal Rubrene

Supravat Karak, Jung Ah Lim, Sunzida Ferdous, Volodimyr V. Duzhko, and Alejandro L. Briseno**

Rubrene single crystals can serve as a model material platform for studying the intrinsic photophysical processes in organic semiconductors and advance our understanding of material functionality in organic photovoltaic applications. The high degrees of structural order and material purity of organic single crystals enable a level of study that is unattainable in materials of current practical importance. Here, the photovoltaic effect at the Schottky interface of rubrene single crystal–aluminum electrode is demonstrated in a lateral ITO–rubrene–Al device geometry. The mechanism of the effect formation is explained based on the reconstructed energy band diagram of the ITO–rubrene–Al heterostructure. In particular, the open circuit voltage (V_{OC}) of the devices shows a strong dependency on the interfacial band bending and corresponding built-in potential at the rubrene–Al Schottky interface. Initially, the photovoltage is found to be equal to the built-in potential at the Schottky interface defined by the work function difference between the bulk of rubrene and the Al electrode, that is, following the Schottky–Mott model. A good agreement is found between the systematically varied built-in potential and the resulting photovoltage magnitude upon insertion of an ultrathin LiF interlayer between the rubrene and Al electrode.

1. Introduction

Organic photovoltaic (OPV) cells have received significant attention in recent years as a new generation of low cost energy sources. The power conversion efficiencies have steadily improved to well over 9%.[1] However, for OPVs to contribute to practical energy needs, higher device efficiencies will be required. While significant research efforts have been focused on optimizing material properties and device architectures, the fundamental physical processes in photovoltage and photocurrent generation have not been fully understood. To be able to design efficient devices, it is important to understand the intrinsic optoelectronic properties of organic semiconductor materials. From a fundamental point of view, organic single crystals with minimized molecular disorder enable the observation of a broad range of intrinsic properties of organic semiconductors. For example, organic single crystal field-effect transistors have been well studied to elucidate the charge transport properties and their crystallographic orientation dependency in rubrene.[2–4] It was also recently demonstrated that rubrene single crystals exhibit anisotropic elastic constants with the stiffest constant along the pitch angle of the crystal structure.[5] Tseng et al. reported tetracene single-crystal solar cells that exhibited anisotropic power conversion efficiencies along the [001] crystal axis.[6] More recently, Podzorov and coworkers reported that triplet excitons can diffuse over several microns in rubrene, which was comparable to the light absorption length.[7] Finally, selective patterning of organic single crystals enables one to envision utilization of the single crystal arrays in high performance organic electronic applications.[8]

Although organic Schottky devices exhibit low power conversion efficiencies because of inefficient charge generation,[9] the simple structure provides a promising model system to study interfacial charge transfer,[10] exciton diffusion[11–13] and influence of interfacial energy levels on cell performance.[14,15] In particular, considering that organic crystals have minimal structural defects and grain boundaries in which exciton quenching is induced, Schottky devices based on rubrene crystals are useful to study intrinsic photovoltaic properties of organic semiconductors. Moreover, the interface of organic semiconductors and the metal is an integral part of electronic devices. In addition to the role of metals as ohmic contacts in conventional field-effect transistors, operation of less common device architectures for organic materials, such as Schottky contact devices that mimic operation of common metal-semiconductor field-effect transistors (MESFET) on inorganic semiconductors, is entirely based on the properties of organic semiconductor/metal interface.[16,17] Therefore, valuable information regarding the fundamental properties of organic semiconductors can be gained from the studies of organic single crystal-metal interfaces.

In this study, we demonstrate a photovoltaic effect at the rubrene–Al and rubrene–LiF/Al interfaces in lateral

---

Dr. S. Karak, Dr. J. A. Lim,[+] S. Ferdous,
Prof. V. V. Duzhko, Prof. A. L. Briseno
Department of Polymer Science and Engineering
University of Massachusetts, Amherst, MA, 01003, USA
E-mail: duzhko@mail.pse.umass.edu;
abriseno@mail.pse.umass.edu
[+]Present Address: Future Convergence Research Division,
Korea Institute of Science and Technology, Hwarangno 14-gil-5, Seoul
136-791, Korea

DOI: 10.1002/adfm.201301891

ITO–rubrene–Al and ITO–rubrene–LiF/Al device configurations. We show that the effect arises at the heterointerface of rubrene with Al and the magnitude of photovoltage can be significantly increased by the insertion of a thin LiF interlayer. We constructed energy band diagrams of these heterostructures based on ultraviolet photoelectron spectroscopy (UPS) and capacitance–voltage (C–V) measurements. This enabled us to explain the mechanism of the photovoltaic effect in detail, including quantitative characteristics, as well as to describe how the electronic structure of the interface between rubrene and the Al electrode is formed.

2. Results and Discussion

Charge transport in rubrene single crystals is anisotropic[3] and the largest charge carrier mobility is along the slip-stack direction referred to as the "b"-axis.[2] In this study, we chose to fabricate planar ITO–rubrene–Al and ITO–rubrene–LiF/Al devices instead of a traditional sandwich-type configuration to allow the photo-generated charges to migrate along the in-plane direction that coincides with high mobility direction in rubrene crystals. The optical image of a device and the schematic cross-section are shown in **Figure 1**(a) and (b), respectively. To localize the region of photocurrent and photovoltage generation in such a device, the current–voltage (I–V) characteristics for both top- and bottom-side illumination were measured (Figure 1c). In general, there are three different regions where the photo-generated excitons can dissociate: at the ITO–rubrene interface (A_1), inside the crystal bulk (A_2), and at the rubrene–Al interface (A_3). When illumination is performed through the ITO glass, that is, from bottom, all three sites are exposed to light (Figure 1b). Alternatively, for top-side illumination, the photocurrent can be generated at the interface with ITO or in the crystal bulk only since the 100-nm thick Al electrode is completely opaque. Although a small photocurrent is generated with the top-side illumination, the photocurrent generation through bottom illumination is much larger. This indicates that excitons dissociate near or at the rubrene–Al interface. Therefore, the planar device geometry allowed distinguishing the region of photocurrent generation.

To investigate the photovoltaic effect at the Schottky interface of rubrene and Al in more detail, we inserted an ultrathin LiF interlayer between the rubrene and Al contact and systematically changed its thickness from 0.5 nm to 3.5 nm. The representative I–V characteristics of such devices under AM 1.5 (100 mW/cm^2) simulated solar irradiation are shown in **Figure 2**. Interestingly, the V_{OC} is found to increase with an increase of LiF thickness. Initially, the device without any LiF interlayer exhibited a V_{OC} of about 0.47 V while it increases up to 1.16 V and 1.28 V for 1.5 nm and 3.5 nm of LiF thickness, respectively. These results imply that the electronic structure of the interface between rubrene and the Al Schottky contact is mainly controlling the photovoltaic effect of the devices. Note that the calculation of photocurrent densities is not straightforward for a two-dimensional geometry of planar devices and, therefore, the photocurrents for different devices cannot be compared directly. Additionally, since the cross-section area for current flow and illumination area are different, calculations of the device power conversion efficiencies are non-trivial too. In order to understand the mechanism of the photovoltaic effect formation and to quantitatively characterize it, primarily the magnitude of open circuit voltage, the results of UPS and C–V measurements will be discussed next.

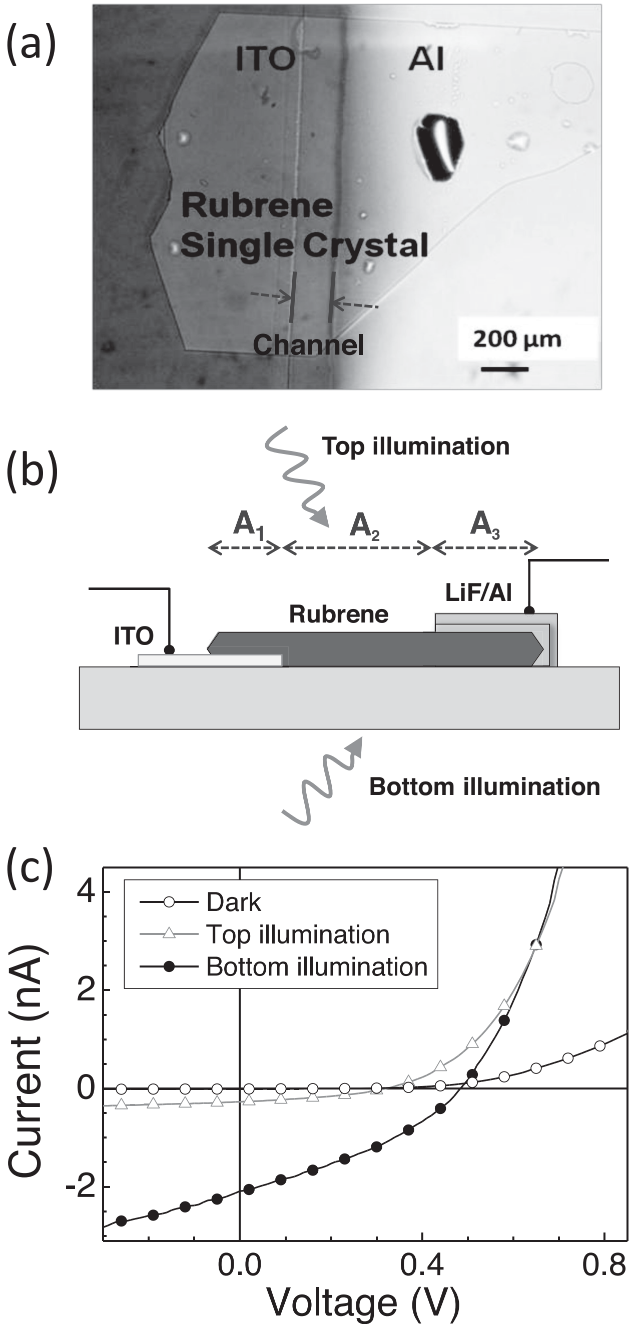

Figure 1. Lateral ITO–rubrene–Al and ITO–rubrene–LiF/Al devices. a) Top view optical image and b) cross-section view of the ITO–rubrene–LiF/Al device configuration, and c) current–voltage characteristics of the ITO–rubrene–Al device in the dark (open circles) and under top- (open triangles) and bottom-side (solid circles) illumination.

UPS was employed to determine the intrinsic energy levels of rubrene as well as the energy level alignment at

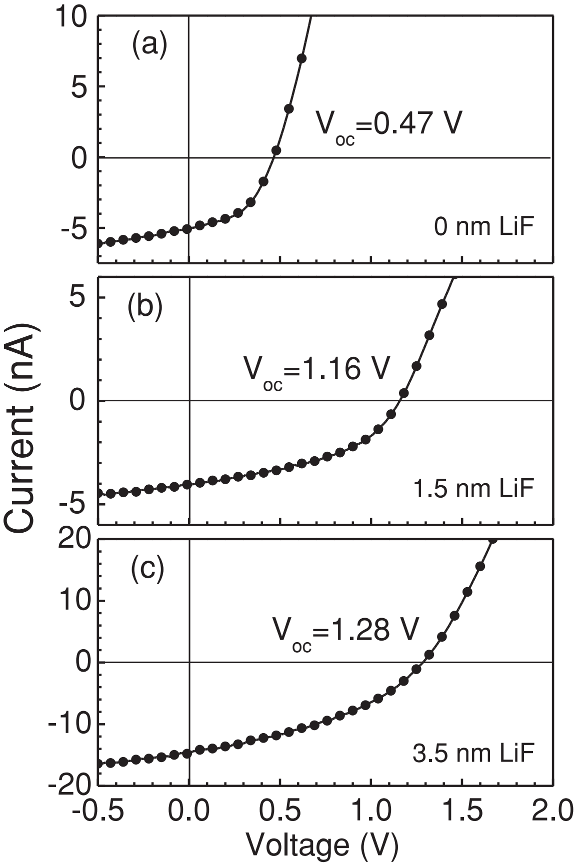

Figure 2. Current-voltage characteristics of devices under AM 1.5 (100 mW cm^{-2}) simulated solar irradiation for different thicknesses of LiF interlayers: a) without LiF, b) 1.5 nm, and c) 3.5 nm of LiF.

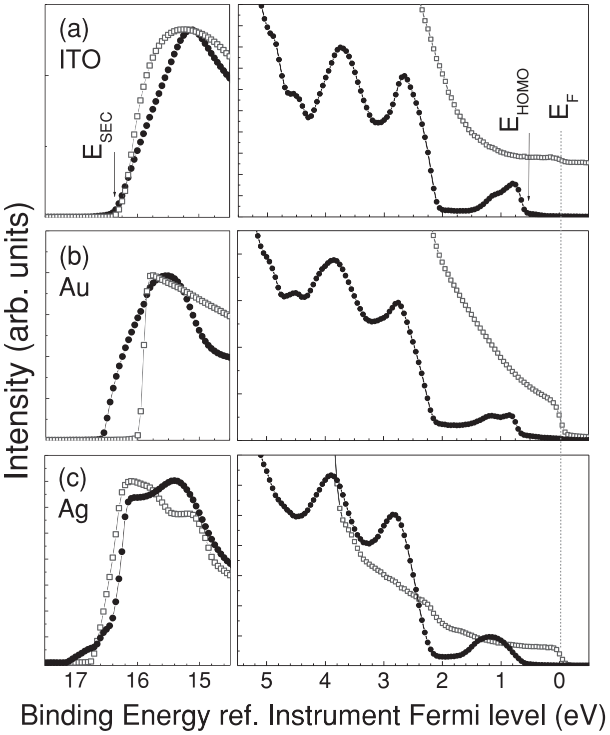

Figure 3. The UPS spectra of rubrene (solid symbols) on a) ITO, b) Au, and c) Ag substrates and the spectra of respective substrate materials (open symbols). Left panels show the energy region near the secondary electron cut-off, the right panels: near the Fermi or HOMO levels. The spectra near the secondary electron cut-off were normalized to their respective peaks and the spectrum of ITO (a, right panel) was shifted vertically for clarity.

the interfaces of rubrene with various electrodes. **Figure 3** shows the UPS spectra of rubrene on ITO, Au and Ag substrates. The UPS spectra have two onsets. The onset energy in the range of high binding energies (left panels) is denoted as E_{SEC}, the onset energy in the range of low binding energies (right panels), denoted E_F or E_{HOMO} for materials with a metal- or semiconductor-like structure of electronic density of states, respectively. The increase of UPS signal intensity around the E_{SEC} corresponds to the excitation of electrons from deep electronic states up to a vacuum level (E_{VAC}). Therefore, the E_{VAC} position (zero of binding/kinetic energy on the absolute energy scale) with respect to the energy scale of the instrument can be calculated as $E_{VAC} = E_{SEC}$-21.2 eV. The low-binding energy onset of the UPS spectrum corresponds to the excitation of electrons from the highest occupied electronic states in the material, i.e. E_F in a metal (considering a zero-temperature approximation which neglects the Fermi-Dirac distribution) or E_{HOMO} in a semiconductor. The energy difference between the E_{VAC} and the E_F/E_{HOMO} is equal to the work function of a metal (Φ) or the ionization potential (*IP*) of a semiconductor. For the heterointerface between the two materials, the difference between their E_{SEC} energies is equal to the difference in E_{VAC} levels which is defined as an interface dipole (Δ).

The low-binding energy parts of the UPS spectra (Figure 3, right panels) for rubrene on all measured substrates appear similar to one another. The peaks at 2.8 eV and 4 eV are the lowest binding energy features of the gaseous phase of rubrene[18] and therefore are the features of non-interacting molecules. The two peaks in the range of lower binding energies, at 0.8 eV and 1.2 eV, are the signature of a condensed phase. They were previously assigned to the highest-occupied-molecular-orbital (HOMO) band of rubrene.[19,20] The measurements of an ionization potential of rubrene resulted in values of 5.2 eV on Au, 5.25 eV on Ag and 5.35 eV on ITO. Since the energy resolution of our UPS instrument is 0.1 eV, this variation can be considered within the instrument resolution. The measured *IP* of rubrene is in good agreement with previous studies.[19,21,22]

Scheme 1 shows the schematic illustration of energy levels of rubrene on a) ITO, b) Au, and c) Ag that were obtained by the quantitative analysis of respective UPS spectra (Figure 3) as described above. The LUMO energy at 2.3 eV above the HOMO was taken from the optical band gap (E_G) of rubrene single crystals[23] measured by the UV-VIS absorption spectroscopy. The interfacial dipoles $\Delta_{ITO} = 0.1$ eV, $\Delta_{Au} = 0.6$ eV, $\Delta_{Ag} = -0.2$ eV for rubrene on ITO, Au and Ag surfaces, respectively, were determined. We note that we performed UPS measurements on

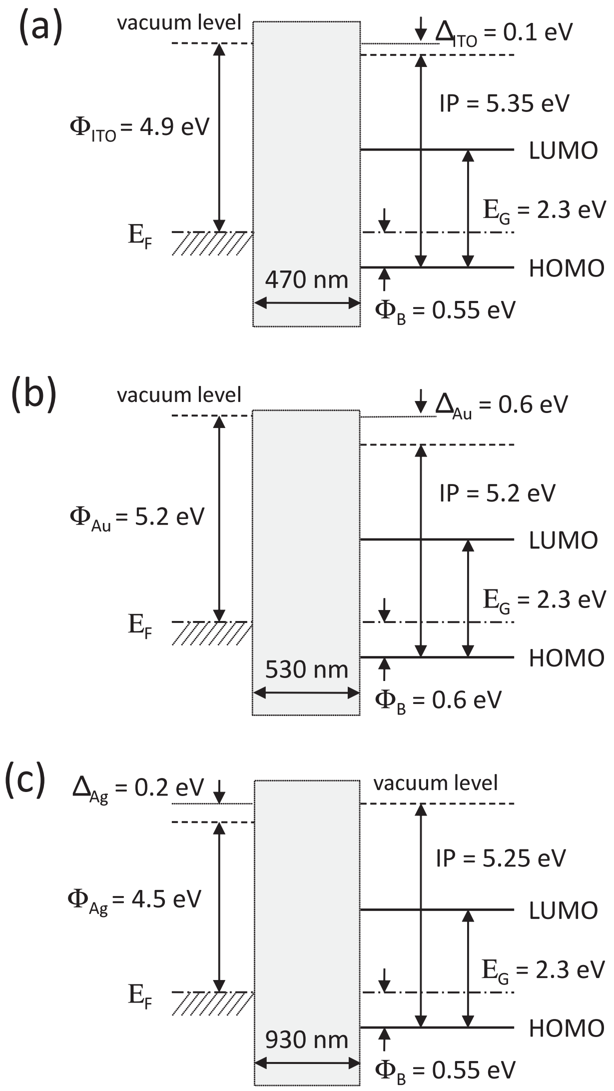

Scheme 1. Schematic illustration of energy levels of rubrene on a) ITO, b) Au, and c) Ag surfaces.

relatively thick films (<1 μm) of single crystal rubrene, unlike the previous studies of ultrathin films where different values of an interfacial dipole and a Fermi level on the same metal surfaces were found.[21,22] On the other hand, our films are much thinner than 20 μm-thick rubrene crystals[19] which allowed us avoiding any charging effects. However, since the UPS technique probes just few surface monolayers, the disadvantage of using such crystals is that the interfacial electronic structure of rubrene with the substrates cannot be probed directly. If the space charge and depletion region exist at the interfaces with ITO, Au or Ag, the indicated Δ values would be a sum of an interfacial dipole and a built-in potential. Therefore, the indicated energy levels refer to the crystal surface.

The most interesting feature of the interfaces of rubrene single crystals with different materials is the position of a Fermi level in the band gap. The E_F is located at 0.55 eV above the HOMO onset and is independent of the used substrate materials (ITO, Au, or Ag). Since the optical band gap of rubrene is 2.3 eV, the position of the Fermi level significantly closer to the HOMO band indicates that rubrene is a doped, p-type material. We would like to note that the transport gap which is slightly larger than the optical gap,[24] would give an alternative approximation of the LUMO onset. Using the transport gap, the Fermi level will be positioned even further away from the middle of the band gap, that is, from the energy where the Fermi level of an intrinsic semiconductor is located. This result is unlike the respective features in the UPS spectra of the ultrathin rubrene films[22] that were evaporated in-situ, i.e., not exposed to air, and that could have different morphology. The origin of doping which shifts the Fermi level has not been addressed in this work. Previously, electronic states at 0.25–0.35 eV above the HOMO were identified and assigned to oxygen doping,[23,25,26] while the structural defects were found to facilitate the oxidation.[27] However, the structural defects were discussed as the sole origin of the same features in the photoluminescence spectra too.[28] The origin of doping in general, and the role of oxidation and structural defects in particular, still remain a matter of debate therefore. Also, since most experimental techniques that were utilized for such studies are sensitive predominantly to the surface properties, an extreme caution needs to be exercised when relating their results to description of the bulk properties.

Illumination of the lateral photovoltaic devices from the bottom indicates that the photovoltaic effect originates at the rubrene–Al interface. Unfortunately, this interface cannot be characterized by the UPS directly since Al quickly oxidizes in air and in-situ fabrication was not possible. The lamination of rubrene onto oxidized surface would result in significantly different interfacial properties comparing to the device fabrication case when Al is thermally evaporated onto rubrene. Therefore, C–V measurements were carried out to extract characteristics of the rubrene–Al and rubrene–LiF/Al interfaces.

When a metal forms contact with a semiconductor, the thermodynamic equilibrium requires that the two materials share a common Fermi level. The associated charge redistribution between the semiconductor, surface/interfacial states and a metal leads to a formation of a depletion region in the semiconductor. From the C–V measurements of a metal–semiconductor junction, the ionized acceptor concentration N_A, the built-in potential V_{bi} and the depletion layer width w can be obtained. For an abrupt junction, the junction capacitance per unit area is given as [29,30]

$$C = \sqrt{\frac{q\,\varepsilon_0 \varepsilon N_A}{2(V_{bi} - V)}} \qquad (1)$$

where q is electronic charge, ε_0 is vacuum permittivity, and ε is relative permittivity of rubrene. Equation 2 describes a linear variation of $1/C^2$ with voltage in the voltage range $V < V_{bi}$.

$$\frac{1}{C^2} = \sqrt{\frac{2(V_{bi} - V)}{q\,\varepsilon_0 \varepsilon N_A}} \qquad (2)$$

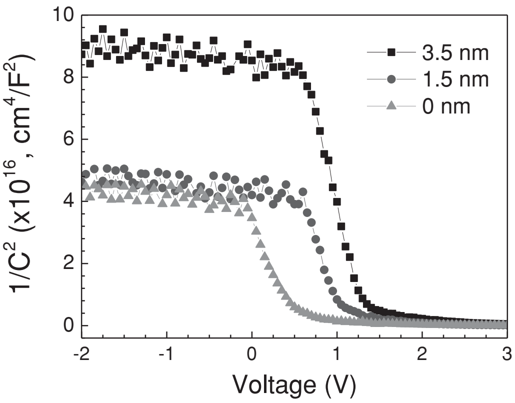

Figure 4. The $1/C^2$ as a function of applied bias (V) for the devices with different thicknesses of LiF interlayer measured at a frequency of 500 Hz.

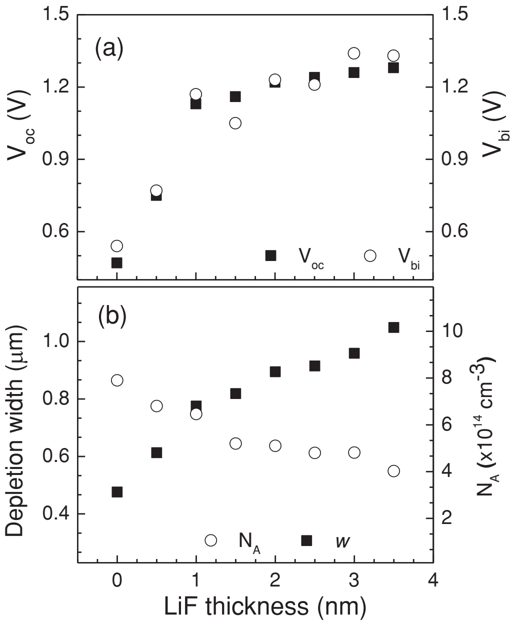

Figure 5. Variation of a) open circuit voltage (V_{OC}) and built-in potential (V_{bi}), and b) depletion layer width (w) and density of acceptor levels (N_A) as a function of LiF interlayer thickness.

The low frequency (500 Hz) $1/C^2$-V plot is shown in **Figure 4** for devices with varying thicknesses of LiF interlayer and an effective device area of 2 mm^2. The capacitance of a metal–semiconductor interface is dominated by the capacitance of the depletion region under reverse bias (negative voltages, Figure 4) and by the diffusion capacitance under forward bias (positive voltages, Figure 4). Since we used single crystal rubrene in a thin-film, sandwich-type geometry to avoid the contribution of the bulk capacitance in series with the depletion region capacitance, the constant level in the C–V curves under negative bias corresponds to a geometrical capacitance of the fully depleted film. A minority carrier injection dominates the diffusion capacitance under large positive bias. In the respective transition regions, the results showed a good linear variation of $1/C^2$ with applied voltage. From the slope of $1/C^2$ versus V curve, the ionized acceptor density N_A is calculated and from the extrapolated intercept (at $1/C^2 = 0$) the built-in potential V_{bi} is measured. **Figure 5**(a) shows the variation of V_{bi} and V_{OC} with change in the interlayer LiF thickness. The V_{OC} values were obtained from the respective I–V curves. Interestingly, we found that V_{bi} showed almost exact trend as we observed for V_{OC}. The built-in potential V_{bi_Al} is equal to 0.5 V for Al interface, and gradually increases as the LiF interlayer becomes thicker saturating at ≈1.35 V as the thickness of LiF layer reaches 3.5 nm. An excellent agreement between V_{bi} and V_{OC} proves that the photovoltaic effect arises at the interface of rubrene with Al.

The calculated values of N_A and V_{bi} are used to obtain the width of the depletion layer w by using the following equation:

$$w = \sqrt{\frac{2\varepsilon_0 \varepsilon (V_{bi} - V)}{q\, N_A}} \tag{3}$$

The variation of w and N_A with LiF thickness within the crystal is shown in Figure 6b. An increase in the built-in potential for thicker LiF layer is accompanied by the increase of the depletion layer width from 0.47 μm for rubrene-Al interface to 1.05 μm for rubrene/LiF (3.5 nm)/Al interface. It is important to note that for larger thickness of LiF interlayer nearly the full crystal is depleted in the sandwich configuration. Such depletion width is comparable to the value for the interface with Indium,[16] which has a similar work function of 4.2 eV. However the depletion width is smaller than the value reported in the other study of rubrene-Al interface[17] where a completely depleted 2 μm-thick films were discussed. The ionized acceptor density N_A is calculated to be around 7.9×10^{14} cm^{-3} for rubrene-Al interface and slightly decreases to 4.02×10^{14} cm^{-3} for 3.5 nm of LiF layer thickness, consistent with a previous study in MESFET geometry.[16] Since the depletion region extends further into the bulk of rubrene for thicker LiF interlayers, the smaller ionized acceptor density for larger LiF thicknesses indicates a non-uniform N_A profile with larger densities near the surface. Approximating the density of states in the HOMO band (N_V) by the molecular density 1.8×10^{21} cm^{-3} in rubrene (Ref. [31]), the $E_F = 0.375$ eV can be estimated. The values of 0.33 eV and above 0.45 eV were previously extracted from the MESFET and temperature-dependent space-charge-limited-current measurements, respectively.[16,25] Our E_F value of 0.55 eV that was directly measured with UPS could be overestimated therefore. This overestimation can result from the experimental procedure how a single energy value as the HOMO onset ($IP = E_{HOMO}$ and, therefore, E_{HOMO}-E_F distance) was assigned for a broad distribution of HOMO states.

Scheme 2 summarizes the energy band diagrams of the ITO–rubrene–Al and ITO–rubrene–LiF/Al heterostructures that were constructed from the UPS and C–V measurements. The interface of rubrene with ITO was already described in Scheme 1a. Scheme 2a shows the energy band diagram of ITO–rubrene–Al interface where a built-in potential eV_{bi_Al} = 0.5 eV of rubrene–Al from the CV measurements is included. When the heterostructure is formed upon Al deposition, the thermodynamic equilibrium requires that the Fermi levels of

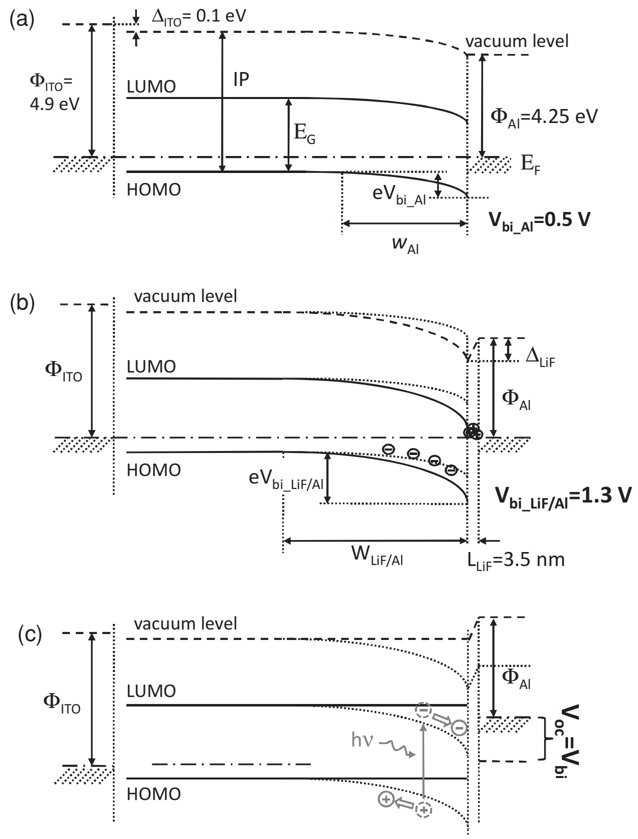

Scheme 2. Energy band diagrams of a) ITO–rubrene–Al heterostructure in the dark, b) ITO–rubrene–LiF/Al heterostructure in the dark, and c) ITO–rubrene–LiF/Al heterostructure under illumination with a photon energy $h\nu > E_G$.

all materials align. A potential drop of 0.65 eV, equal to the difference in the Fermi levels of two electrodes, 4.9 eV for ITO and 4.25 eV for Al, should be redistributed over the bulk of rubrene. Since there is a drop of 0.1 eV across the rubrene–ITO interface due to the interfacial dipole and/or the built-in potential, the fact that the remaining 0.55 eV is nearly equal to the built-in potential of 0.5 eV indicates that rubrene–Al interface formation follows a Schottky–Mott model, that is, an ideal case for the semiconductor–metal energy-level alignment.[29] Neither the interfacial dipole nor the surface states that can pin the Fermi level are found to play any role at the rubrene–Al interface.

An improved performance of organic light-emitting diodes and photovoltaic cells when an ultrathin LiF layer is inserted in-between the cathode and organic active layer has been previously reported.[32,33] The LiF interlayer reduces the electron injection barrier which leads to higher injection currents in OLEDs.[32] Similar to the reported results here, there are numerous demonstrations that LiF leads to a larger open circuit voltage in OPVs.[33] This has been attributed to the reduced work function of Al upon deposition of ultrathin LiF layers,[34] though several other mechanisms have been proposed as well.[35] In Scheme 2b, the reduced work function of Al electrode is shown as an interfacial dipole Δ_{LiF}. Though the interfacial dipoles are usually assigned to the sharp interface between the two materials, since it takes a certain thickness of LiF to form a continuous layer, we show the interfacial dipole as a potential drop across the entire LiF layer thickness. As follows from Figure 5, the insertion of ultrathin LiF interlayer between the rubrene and Al electrode increases the magnitude of a built-in potential $eV_{bi\_LiF/Al}$ to 1.3 eV, corresponding to a difference of ~0.8 eV with the case when no LiF is present.

The mechanisms of exciton dissociation, free carrier and polaron generation in rubrene single crystals have been previously studied.[36,37] Under illumination with photons of sufficiently large energy $h\nu \geq E_G$, the polarons can be formed directly from free charges as well as generated through the subsequent exciton dissociation. It should be noted, however, that the quantum yields of exciton dissociation and free carrier generation are typically very low in organic semiconductors. After photogeneration, the free charges of opposite signs will be spatially separated in the built-in electric field of interfacial space charge region – electrons will be collected by the Al electrode and holes will move towards the ITO electrode (Scheme 2c). Since rubrene was found to be a p-type material, holes are the majority carriers and, therefore, they can diffuse over large distance in the bulk without recombination. Moreover, in the lateral device geometry the holes move along the most efficient *b* direction.[2] The separation of photo-generated electron and holes in space will lead to the flattening of bands and formation of a photovoltage. Therefore, at large illumination intensities, the photovoltage can be as large as the magnitude of a built-in potential. Once the bands are flat, the photogenerated charges recombine without spatial separation. The equal V_{bi} and V_{OC} for rubrene-Al and rubrene-LiF/Al interfaces completely support this model.

3. Conclusions

In this study, we demonstrated a photovoltaic effect at the ITO–rubrene–Al and ITO–rubrene–LiF/Al devices with lateral device geometry. A combination of UPS and C–V analysis allowed constructing the energy band diagrams of the heterointerfaces. The band diagrams have been used to describe the mechanism of the photovoltaic effect formation. In all cases, the magnitude of photovoltage was found to be equal to the built-in potential at the rubrene and Al or LiF/Al interfaces. Single crystal rubrene grown by physical vapor transport process and briefly exposed to air was found to be an unintentionally doped, p-type material with the Fermi level at 0.55 eV above the HOMO band. The built-in potential at the rubrene interface with Al equals the work-function difference between the ITO and Al electrodes, following the Schottky–Mott model. Insertion of LiF interlayer significantly increases the built-in potential and is consistent with the mechanism that deposition of LiF reduces the work function of Al. We gave a comprehensive description of the interface formation between rubrene and Al as well as discussed the role of LiF interlayers.

4. Experimental Section

Samples for I–V and C–V Measurements: Rubrene single crystals were grown by precise control of physical vapour transport process.[38] Thin single crystals with thicknesses up to 1 μm were selected. Selected crystals were then laminated on the patterned ITO substrates (Thin Film Devices, surface resistivity 20 Ω cm) pre-cleaned with detergent, de-ionized water, acetone, and isopropyl alcohol by an ultrasonic cleaner followed by 5 min oxygen-plasma treatment. Lithium fluoride (LiF) and aluminium (Al) are sequentially deposited as a cathode to fabricate different device structures such as lateral and conventional sandwich-type architectures. For lateral geometry, LiF and Al were deposited using a shadow mask with a ≈200 μm gap from ITO. Rubrene crystals were positioned with a long axis (that corresponds to crystallographic b-axis) across the anode and cathode as shown in Figure 1a. For sandwich structure, the cathode materials were directly deposited on the crystals. The lateral geometry samples were used for conventional I–V measurements, whereas the sandwich-type samples were used for CV measurements.

Samples for UPS Measurements: ITO substrates were cleaned similarly as described above right before the measurements. Au, Ag and Al films were thermally evaporated onto a highly-doped n^{++}-Si substrate (Phosphorous doped, 0.005 Ωcm resistivity) using a thermal evaporator inside of a glove box (N_2, <1 ppm of O_2, <1ppm of H_2O), and transferred between the glove box and UPS instrument inside of a nitrogen container with a <30 s exposure to air. Comparing to the workfunctions of Ar^+-sputtered surfaces, more prolonged exposure to air would lead to a slightly decreased work function of Au (5.3 eV for sputtered surface) and increased work function of Ag (4.45 eV for sputtered surface). Exposure of Al drastically changed its workfunction, therefore rubrene crystals were not laminated onto Al and only thermally evaporated Al on rubrene is discussed. Rubrene single crystals were laminated onto ITO or Au directly, or using the isopropanol vapors on Ag surface immediately after moving the substrates out of the glove box. The film thickness was measured by the surface profiler (KLA Tencor, model Alpha-Step IQ).

Electrical Measurements: The current–voltage (I–V) characteristics of the devices were measured under AM 1.5 (100 mW/cm^2) simulated solar irradiation conditions using a Keithley 4200-SCS measurement unit together with a Newport 67005 solar simulator. The capacitance–voltage measurements for different samples were carried out using a Solartron SI-1260 impedance/gain phase analyzer at the frequency of 500 Hz. All the device characterizations have been carried out under ambient conditions at room temperature.

Ultraviolet Photoelectron Spectroscopy: The UPS measurements were performed with the electron spectroscopy for chemical analysis instrument (Omicron Nanotechnology, model ESCA+S) at a base pressure of 4×10^{-10} mbar. The instrument configuration consisted of a Helium discharge lamp (He I line, 21.2 eV) as the UV excitation source and a hemispherical SPHERA energy analyzer. The illumination source and energy analyzer were at angles of 35° and 90°, respectively, with respect to the sample surface plane. All the measurements were carried out at a –3 V sample bias to collect the low kinetic energy electrons. The resolution of the UPS instrument was 0.1 eV as determined from the width of the Fermi level of silver cleaned by Ar^+ sputtering.

Acknowledgements

S. K. and J.A.L.A. Lim contributed equally to this work. S.K. and A.L.B. acknowledge support by the Office of Naval Research (N000141110636). J.L. L acknowledges support from the University of Massachusetts start-up funds. Spectroscopic characterization was carried out using facilities supported as part of Polymer-Based Materials for Harvesting Solar Energy, an Energy Frontier Research Center funded by the US Department of Energy, Office of Basic Energy Sciences under Award Number DE-SC0001087.

Received: June 3, 2013
Revised: August 5, 2013

[1] Z. He, C. Zhong, S. Su, M. Xu, H. Wu, Y. Cao, *Nature Photonics* **2012**, *6*, 591.
[2] V. Podzorov, E. Menard, A. Borissov, V. Kiryukhin, J. A. Rogers, M. E. Gershenson, *Phys. Rev. Lett.* **2004**, *93*, 086602.
[3] V. C. Sundar, J. Zaumseil, V. Podzorov, E. Menard, R. L. Willett, T. Someya, M. E. Gershenson, J. A. Rogers, *Science* **2004**, *303*, 1644.
[4] C. Reese, Z. Bao, *Adv. Mater.* **2007**, *19*, 4535.
[5] M. A. Reyes-Martinez, A. Ramasubramaniam, A. L. Briseno, A. J. Crosby, *Adv. Mater.* **2012**, *24*, 5548–5552.
[6] R. J. Tseng, R. Chen, V. C. Tung, Y. Yang, *Adv. Mater.* **2008**, *20*, 435.
[7] H. Najafov, B. Lee, Q. Zhou, L. C. Feldman, V. Podzorov, *Nature Mater.* **2010**, *9*, 938.
[8] A. L. Briseno, S. C. B. Mannsfeld, M. M. Ling, S. H. Liu, R. J. Tseng, C. Reese, M. E. Roberts, Y. Yang, F. Wudl, Z. N. Bao, *Nature* **2006**, *444*, 913–917.
[9] C. J. Brabec, N. S. Sariciftci, J. C. Hummelen, *Adv. Funct. Mater.* **2001**, *11*, 15–26.
[10] I. G. Lezama, M. Nakano, N. A. Minder, Z. Chen, F. V. D. Girolamo, A. Facchetti, A. F. Morpurgo, *Nature Mater.* **2012**, *11*, 788–794.
[11] A. K. Ghosh, T. Feng, *J. Appl. Phys.* **1978**, *49*, 5982–5989.
[12] D. Kurrle, J. Pflaum, *Appl. Phys. Lett.* **2008**, *92*, 133306.
[13] S. Banerjee, A. P. Parhi, S. S. K. Iyer, S. Kumar, *Appl. Phys. Lett.* **2009**, *94*, 223303.
[14] M. L. Zhang, Irfan, H. J. Ding, Y. L. Gao, C. W. Tang, *Appl. Phys. Lett.* **2010**, *96*, 183301.
[15] T. Taima, M. Chikamatsu, R. N. Bera, Y. Yoshida, K. Saito, K. Yase, *J. Phys. Chem. B.* **2004**, *108*, 1.
[16] T. Kaji, T. Takenobu, A. F. Morpurgo, Y. Iwasa, *Adv. Mater.* **2009**, *21*, 3689–3693.
[17] D. Braga, M. Campione, A. Borghesi, G. Horowitz, *Adv. Mater.* **2010**, *22*, 424–428.
[18] N. Sato, K. Seki, H. Inokuchi, *J. Chem. Soc., Faraday Trans. 2* **1981**, *77*, 1621–1633.
[19] S. I. Machida, Y. Nakayama, S. Duhm, Q. Xin, A. Funakoshi, N. Ogawa, S. Kera, N. Ueno, H. Ishii, *Phys. Rev. Lett.* **2010**, *104*, 156401.
[20] A. Vollmer, R. Ovsyannikov, M. Gorgoi, S. Krause, M. Oehzelt, A. Lindblad, N. Martensson, S. Svensson, P. Karlsson, M. Lundvuist, T. Schmeiler, J. Pflaum, N. Koch, *J. Electron Spectrosc. Relat. Phenom.* **2012**, *185*, 55.
[21] L. Wang, S. Chen, L. Liu, D. Qi, X. Gao, A. T. S. Wee, *Appl. Phys. Lett.* **2007**, *90*, 132121.
[22] H. Ding, Y. Gao, *Appl. Phys. A* **2009**, *95*, 89–94.
[23] O. Mitrofanov, D. V. Lang, C. Kloc, J. M. Wikberg, T. Siegrist, W.-Y. So, M. A. Sergent, A. P. Ramirez, *Phys. Rev. Lett.* **2006**, *97*, 166601.
[24] D. R. T. Zahn, G. N. Gavrila, M. Gorgoi, *Chem. Phys.* **2006**, *325*, 99.
[25] C. Krellner, S. Haas, C. Goldmann, K. P. Pernstich, D. J. Gundlach, B. Batlogg, *Phys. Rev. B* **2007**, *75*, 245115.
[26] W.-Y. So, J. M. Wikberg, D. L. Lang, O. Mitrofanov, C. L. Kloc, T. Siegrist, A. M. Sergent, A. P. Ramirez, *Solid State Commun.* **2007**, *142*, 483.
[27] R. J. Thompson, S. Fearn, K. J. Tan, H. G. Cramer, C. L. Kloc, N. J. Curson, O. Mitrofanov, *Phys. Chem. Chem. Phys.* **2013**, *15*, 5202.
[28] Y. Chen, B. Lee, D. Fu, V. Podzorov, *Adv. Mater.* **2011**, *23*, 5370.
[29] S. M. Sze, *Physics of Semiconductor Devices*, Wiley, New York **1981**, Ch. 5.
[30] E. H. Rhoderick, R. H. Williams, *Metal–Semiconductor Contacts*, Clarendon Press, Oxford **1988**, Ch. 4.
[31] W. Xie, C. D. Frisbie, *J. Phys. Chem. C* **2011**, *115*, 14360.
[32] L. S. Hung, C. W. Tang, M. G. Mason, *Appl. Phys. Lett.* **1997**, *70*, 152.

[33] C. J. Brabec, S. E. Shaheen, C. Winder, N. S. Sarifitci, P. Denk, *Appl. Phys. Lett.* **2002**, *80*, 1288.

[34] R. Schlaf, B. A. Parkinson, P. A. Lee, K. W. Nebesny, G. Jabbour, B. Kippelen, N. Peyghambarian, N. R. Armstrong, *J. Appl. Phys.* **1998**, *84*, 6729.

[35] H. Ishii, K. Sugiyama, E. Ito, K. Seki, *Adv. Mater.* **1999**, *11*, 605.

[36] S. Tao, H. Matsuzaki, H. Uemura, H. Yada, T. Uemura, J. Takeya, T. Hasegawa, H. Okamoto, *Phys. Rev. B* **2011**, *83*, 075204.

[37] H. Najafov, B. Lyu, I. Biaggio, V. Podzorov, *Appl. Phys. Lett.* **2010**, *96*, 183302.

[38] A. L. Briseno, R. J. Tseng, M. M. Ling, E. H. L. Falcao, Y. Yang, F. Wudl, Z. N. Bao, *Adv. Mater.* **2006**, *18*, 2320.